Sub- and supercritical hydrothermal route for the synthesis of xonotlite nanofibers for application to green concrete materials

Valentina Musumeci, Paula Sanz Camacho, Ke Xu, Paulo J.M. Monteiro, Jorge Dolado, Cyril Aymonier

Sub- and supercritical hydrothermal route for the synthesis of xonotlite nanofibers for application to green concrete materials

Valentina Musumeci [ab], Paula Sanz Camacho[a], Ke Xu[cd], Paulo J.M. Monteiro[c], Jorge S. Dolado[be], Cyril Aymonier[a]

[a] *Univ. Bordeaux, CNRS, Bordeaux INP, ICMCB, UMR 5026, F-33600 Pessac, France*
[b] *Centro de Física de Materiales (CSIC-UPV/EHU)-Material Physics Centre (MPC), Paseo Manuel de Lardizabal 5, 20018 San Sebastián, Spain*
[c] *Department of Civil and Environmental Engineering, University of California, Berkeley, CA 94720, USA*
[d] *Computational Research Division, Lawrence Berkeley National Laboratory, Berkeley, CA 94720, USA*
[e] *Donostia International Physics Center, 20018 San Sebastián, Spain*

Abstract

Despite a wide range of applications, naturally occurring minerals suffer from some limitations for industrial use. Consequently, many research efforts have been conducted to develop a fast, optimized, and sustainable methodology to produce synthetic minerals. In the case of calcium silicate hydrates (CSH), the hydrothermal flow approach allows to mimic the environment at high temperature and pressure of the natural geological processes for the synthesis of xonotlite under sub- and supercritical conditions in only few seconds. The ultra-fast, flexible, and effective production of xonotlite particles reported in this work expands its use towards industrial requirements, especially for applications to cement-based materials. In this context, CSH nanominerals can be used to impart new functionality or to accelerate the hydration process of cement for developing green cement materials. This study sheds light on the acceleration effect of crystalline xonotlite seed, measured using isothermal calorimetry and synchrotron radiation based X-ray microtomography, as a means of lowering the cement content without compromising the performance of the paste.

1. Introduction

A natural mineral is defined as a solid with specific chemical composition and a highly ordered atomic arrangement that has been formed as a result of a geological process. From the beginning of civilization, natural minerals have played a key role as raw materials for the social, technological, and economic development of modern society [1]. Among the wide variety found in nature, calcium silicate hydrates are members of a family of minerals that feature layered crystalline structures with different calcium-to-silicon (Ca/Si) ratios. In nature, they form consequently to the geological hydrothermal reactions between basic igneous rocks and hyperalkaline fluids. In the last years, calcium silicate hydrates have been highlighted as

attractive materials due to their potential applicability in numerous fields, such as orthopedic applications [2], insulating materials [3], stabilizing agents for trapping wastewater impurities, and as an addition for reinforced concrete [4]. In the latter case, employing these mineral phases in cement relies on their high chemical compatibility with the calcium silicate hydrate (C-S-H) gel, the main hydration product of cement paste and the primarily responsible for its strength and performance. Nowadays, concrete is the most widely used construction material, and as a consequence of the great quantity of clinker produced, every year, the manufacturing industry of cement accounts for about 7–8% of the global CO_2 anthropogenic emissions [5], [6]. In this context, research for producing more ecological cement is a challenge of fundamental importance to reducing the environmental footprint. The sustainability of concrete can be improved by partially replacing the amount of clinker by different supplementary cementitious materials or enhancing the material performance, making the life cycle of cement structures more resilient and durable. In this context, a significant number of studies have been developed to improve the knowledge of the chemical admixture technology to reduce the cement content without compromising the concrete performance, or even to improve the material mechanical properties [4], [7], [8], [9], [10]. Furthermore, there is great interest in the development of new admixtures to impart new functionalities (i.e., photocatalytic or sensing capabilities) or to modify the hydration process [11], [12]. Several classes of admixtures exist and can be identified depending on their utility and effect on the concrete. Among them, there are water-reducing, setting time-modifiers, which are classified in retarding or accelerating admixtures, *etc*. An interesting category includes additions or chemical admixtures to accelerate the early hydration of cement. These additions play a relevant role in precast structures where speeding up the hydration kinetics allows the removal of the mold and finalizing the structure in shorter times, minimizing the cost of construction. Additionally, accelerators are particularly suitable in a cold environment to avoid the risk of frost damage in the concrete skeleton.

Recent studies have shown the effect of xonotlite, a calcium silicate hydrate mineral, as a seed to trigger the autocatalytic formation of the C-S-H gel [13], [14]. Xonotlite is usually described as having the following formula $Ca_6Si_6O_{17}(OH)_2$ [15]. The basic elements of the xonotlite structure have been identified as CaO-polyhedral layer and Si_6O_{17}-double chains. The Ca-polyhedral layer is composed of three different calcium sites depending on the Ca coordination in the structure. Two of them are seven-fold coordinated by oxygen, whereas the third calcium atom has octahedral coordination. The other basic xonotlite structural elements are Si_6O_{17}-double chains bonded via sheets of edge-sharing Ca-polyhedra. Each Si_6O_{17}-double chains is formed by condensation of two wollastonite-like Si_3O_9-dreier-einfachketten chains [15], [16]. That single unit consists of repetitive silicon-oxygen tetrahedra with a periodicity of three SiO_4. Among them, two are paired together to form Si_2O_7, and the third one corresponds to a single tetrahedron in a bridging position to connect the paired SiO_4. Consequently, in xonotlite, the Si_3O_9 chains are linked together by sharing the apical oxygen atoms of two bridging tetrahedra, forming what is known as Si_6O_{17}-dreier-doppelketten double chain.

Despite a wide range of applications, the employment of natural minerals as xonotlite often suffers from impurities or contaminant phases and limited natural deposits. Therefore, the increase in demand stimulated the search for new and green approaches for sustainable and rapid production at the industrial scale. So far, the hydrothermal methodology represents the most common route for producing synthetic minerals. The conventional hydrothermal synthesis of xonotlite has been investigated, in the literature, in a wide range of temperatures, times, and precursors. The most common temperature ranges between 150 and 250 °C [17]. However, in the case of low temperature, the synthesis time is very long (133 days at 150 °C)

[18], and can be reduced to several hours (~17 h to obtain crystalline single-phase material) at 250 °C [14]. It appears clear that the main disadvantage of this technique relies on the very long synthesis times for synthesizing high crystalline xonotlite particles. In this context, the innovative supercritical hydrothermal flow synthesis (SHFS) represents a breakthrough, allowing producing model nanominerals very close to the natural counterpart in the crystallinity and morphologies [19]. Supercritical water, exhibiting unique thermophysical properties that differ largely from water at ambient conditions, acts as a solvent for mimicking the environments at high temperature and pressure of the geological natural process [1], [20], [21]. In 2018, the synthesis of xonotlite particles in supercritical water was reported by Diez-Garcia et al. [22]. However, in their work, beyond the proof of concept, the study of the structure and the applications of the mineral were limited by the amount of the produced material. Most calcium silicate hydrate minerals have fiber-like morphology, which results in clogging problems from an experimental point of view. Consequently, the first objective of this work is on the design and the development of a more suitable set-up for higher and more effective mineral production. Furthermore, we have conducted a parametric study to identify the effect of temperature, in near- or supercritical conditions, on the crystallinity and structural properties of xonotlite, to then compare them with those reported in the literature so far.

After determining the optimal value parameters for producing pure single-phase xonotlite, we have focused on the employment of the as-produced particles into cement-based materials to partially replace the clinker content into the paste. In this context, our study could open the door to a more flexible and effective production for the industrial uses of xonotlite in several application fields.

2. Experimental

2.1. Materials

Xonotlite nanoparticles were synthesized by an SHFS starting from the following precursors: calcium nitrate tetrahydrate ($Ca(NO_3)_2.4\ H_2O$, purity ≥ 99%) and sodium metasilicate nonahydrate ($Na_2SiO_3.9\ H_2O$, purity ≥ 98%). The precursors were purchased from Sigma Aldrich and used as received.

2.2. Hydrothermal flow synthesis apparatus and procedure

The production of xonotlite nanoparticles was carried out in a continuous reactor. A process flow diagram and a picture of the entire experimental system are shown in Fig. 1. The set-up is composed of three sections: the injection of the chemical precursors, the reactor where the crystallization of the xonotlite nanoparticles occurs, and the product recovery.

To assess the impact of the experimental parameters on the material properties and then to be able to use it in several application fields, a work of process engineering was carried out to design, construct, develop, implement, and monitor the synthesis equipment. Firstly, to avoid any clogging problems, we have decided to scale up a conventional laboratory-scale reactor. The developed supercritical continuous system consists of homemade user-customized equipment composed of several task-specific units, some commercially available and others specially designed, and assembled together. The set-up is highly modular and offers the opportunity to configure the equipment with specific requirements easily.

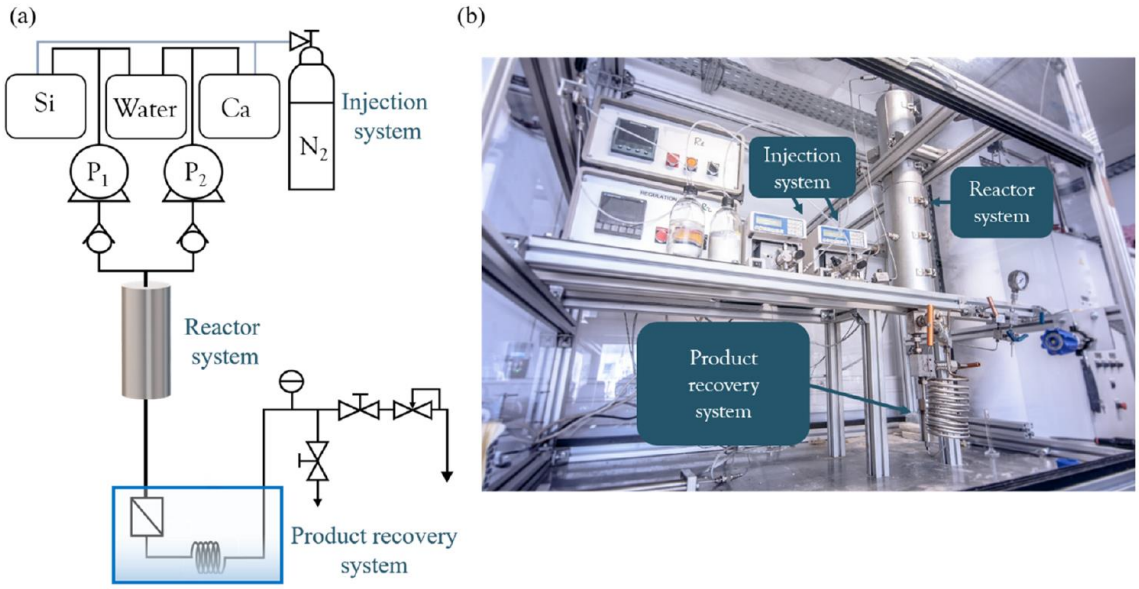

Fig. 1. (a) Schematic representation and (b) picture of the set-up designed and developed in this work for the flow synthesis of xonotlite in near- and supercritical water.

The developed experimental apparatus produces ~2.9 g/h of xonotlite. Behind the high modularity of the system, two more advantages rely on the fine control of the reaction kinetics through the chosen residence times and the possibility of using high molar concentration precursor solutions for effective production of materials without the risk of clogging.

For the synthesis, two precursors solutions were prepared by dissolving a stoichiometric amount (M = 0.1 mol/L) of $Ca(NO_3)_2.4H_2O$ and $Na_2SiO_3.9H_2O$ in pure water to obtain Ca/Si molar ratio = 1. Afterward, the precursor solutions were kept under an N_2 flow using three outlets line equipping the experimental set-up to prevent their carbonation. Initially, only pure water was injected by the two Jasco Isocratic HPLC pumps into the system, and the pressure was progressively increased by closing the BPR. At that time, the system's temperature was increased by setting the operating temperature value on the Eurotherm controllers. When the reactor reached the desired temperature and pressure conditions, the three-way junction valves were turned to switch to the precursor lines. The precursor solutions were pumped at 2.8 mL/min and fed to the heated and pressurized reactor. At the end of the synthesis time, the heating system was shut down, and the reactor was let cool down to room temperature. Finally, once the system returned to ambient conditions, the filter was disassembled from the reactor and opened by a 15-inch adjustable wrench to collect the synthesized particles. The produced materials were dried in an oven at 60 °C overnight before being finely grounded into a powder for the characterization analyses.

2.3. Cement paste preparation

All cement pastes were prepared using ASTM Type I cement at a water-to-binder ratio (w/b) of 0.5 at 25 °C. In the seeded pastes, a variable concentration of dried xonotlite nanoparticles, 0.5 wt% or 1 wt%, per weight of cement was employed. The seeds were dispersed in deionized water and then sonicated for 120 s. Subsequently, the obtained colloidal suspension was added to the cement powder and mixed for 90 s at 800 rpm using a vortex mixer. Lastly, after waiting for 60 s, the slurry was mixed at 1000 rpm for 90 s.

2.4. Materials characterization

2.4.1. Powder X-Ray diffraction (PXRD)

Powder X-ray diffraction patterns were recorded on a PANalytical X'Pert PRO MPD X-ray diffractometer in Bragg-Brentano θ-θ geometry. The employed radiation source, Cu Kα ($K_{\alpha1}$ λ = 1.5418 Å, $K_{\alpha2}$ λ = 1.5444 Å), operated at a generator voltage of 45 kV and a current of 40 mA. Continuous scans were collected by an X'Celerator multi-strip detector within the range 8.012–99.991° (2θ) with a minimum step size of 0.017° (2θ). Before measurement, the samples were finely ground and sieved at 100 µm. Afterward, the powder was placed and uniformly distributed into the sample holder ring to form a flat pellet.

2.4.2. Solid-state nuclear magnetic resonance spectroscopy (SSNMR)

Solid-state nuclear magnetic resonance spectra were acquired on a Bruker Avance 300 MHz spectrometer, equipped with a 7.05 T wide-bore magnet. The experiments were performed at room temperature using a standard 4-mm magic angle spinning (MAS) probe with MAS rates of 10 kHz. For ^{1}H solid-state NMR, a rotor-synchronized Hahn-echo sequence was employed with a π/2 pulse of 2 µs and a recycle delay of 5 s. The chemical shifts refer to ultrapure Milli-Q water (shift: + 4.7 ppm). While, for ^{29}Si solid-state NMR, the spectra were acquired either directly, using a short pulse length of 2.4 µs and a recycle delay of 10 s, or using cross polarization from ^{1}H (^{1}H–^{29}Si CP/MAS NMR) with square contact pulse of 6 ms and a recycle delay of 3 s. In these cases, chemical shifts are referenced relative to silicon oil at - 22 ppm.

2.4.3. Fourier transform infrared spectroscopy (FTIR)

Fourier transform infrared measurements were conducted using a Bruker Equinox 55 spectrophotometer. The spectra were recorded over 32 scans in the spectral absorption region of 400–4000 cm^{-1}, with a spectral resolution of 4 cm^{-1}. Before the analysis, the sample (1 wt%) was dispersed into an appropriate amount of KBr, which is optically transparent within the mid-IR region.

2.4.4. High-resolution Scanning electron microscopy (HR-SEM)

High-resolution field emission gun SEM-FEG HR (JEOL 6700 F) operating at a voltage of 5 kV, working distance of 6 mm and a magnification of 30,000 × or 50,000 × was employed to investigate the morphology of produced xonotlite particles. To carry out a SEM analysis, the dry powder samples (< 2 mg) were dispersed in ethanol, and then placed by drop-casting on an aluminium stub. Before imaging, being xonotlite a non-conductive material, a 1 nm layer of platinum was deposited on the surface through sputter coating.

2.4.5. High-resolution transmission electron microscopy (HR-TEM)

High-resolution transmission electron imaging was performed using a JEOL Jem 2200FS FEG high-resolution microscope, operating at 200 kV with a range of accessible magnification within 4000 × - 600000 × and a resolution of 0.1 nm. Samples for HR-TEM analysis were prepared by drop-casting a suspension of nanoparticles (< 2 mg) in ethanol (∼1 mL) onto a carbon-coated copper grid.

2.4.6. Calorimetry analysis

The calorimetry analysis was employed to measure, over time, the heat released during the hydration process of cement. To carry out the experiments, 5 g of cement paste was placed into a 20 mL hermetic glass

bottle and then loaded into TAM Air isothermal calorimeter within 6 min after the initial contact of clinker with water. The measurements were performed at 25 ± 0.001 °C for 48 h for each sample.

2.4.7. Synchrotron X-ray computed microtomography (µCT)

Synchrotron µCT was performed at beamline 8.3.2 at the Advanced Light Source (ALS) of the Lawrence Berkeley National Laboratory [23]. Each of the as-prepared pastes was loaded into a cylindrical thin-wall polyimide tube (~ 3 mm diameter) to perform the analysis. The cement pastes were tested at different setting times, 7 and 36 h, at ~25 °C. During the measurement, the sample was irradiated by a focused X-ray beam of 40 mm × ~4.6 mm size (at the sample) with an energy of 35 keV. The ring energy was 1.9 GeV to carry out the experiment, and the beam current was maintained constant at 500 mA. The sample was rotated around the axis perpendicular to the X-ray beam propagation at each scan. For each cement paste, a totality of 1969 projected radiographs with an angle step of 0.09° and an exposure time of 20 ms were acquired onto a 5x Mitutoyo magnification optical objective lens and a 2560px PCO.Edge Scientific CMOS camera. Under the above experimental settings, the field of view was 3.3 mm, and the pixel resolution was 1.3 µm/voxel for each scan. During the X-ray computed microtomography experiment, a tomogram with dimensions of 2560*2560*1969 voxels^3 (32-bit, 56.7 GB) was reconstructed using the filtered back projection algorithm [24], [25] for each sample.

3. Results and discussion

The very complex system identified as $CaO\text{-}SiO_2\text{-}H_2O$ is composed of about thirty crystalline phases, characterised by different Ca/Si molar ratios. Most of the minerals belonging to this family can be obtained through hydrothermal route. The formation of one synthetic specie or another depends on the control of numerous parameters, such as the Ca/Si ratio, the time and the temperature of the reaction. Therefore, the synthesis of calcium silicate hydrate minerals is quite challenging due to the difficulty in manufacturing crystalline and pure single phase materials. Several studies in the literature have investigated the mechanism of the xonotlite phase formation via the hydrothermal route [26], [27], [28].

On the basic of previous researches and the results obtained in this work, the synthesis of xonotlite under sub- and supercritical conditions results from two steps.

First, the dissolution of precursors gives rise to the formation of siliceous species (SiO_3^{2-}) which go around positively charged calcium ions (Ca^{2+}) [26]. After rapid reaction, the precipitation at room temperature of the Ca- and Si-precursors in the T-mixing piece at the inlet of the reactor takes place to form a calcium silicate hydrate compound (C-S-H) in the form of gel. This poorly crystalline material is constituted by CaO layers and disordered silicate chains with a good periodicity along the ab plane but a low order along the [001] direction [27]. That C-S-H compound can be considered as the starting precursor for the synthesis of xonotlite under near- and supercritical conditions. In a second stage, inside the tubular reactor kept under near- or supercritical conditions, the CaO layers and silicate chains become more ordered with an increasing of the periodicity along the *c*-direction giving rise to the crystallization of xonotlite particles [27]. The chemical process that results in the formation of crystalline xonotlite starting from calcium nitrate tetrahydrate and sodium metasilicate nonahydrate is described by the following formula:

$$6\ Na_2SiO_3.9H_2O + 6\ Ca(NO_3)_2.4H_2O \rightarrow Ca_6Si_6O_{17}(OH)_2 + 12\ NaNO_3 + 12H_2O$$

To study the chemical process that results in the formation of crystalline xonotlite, syntheses at different temperatures were performed, as will be discussed in the following.

3.1. Crystallization of xonotlite: influence of the synthesis parameters

3.1.1. Influence of temperature

The samples were prepared via hydrothermal flow synthesis at 23.5 MPa and different temperatures: 250, 300, 350, and 400 °C. The syntheses were performed keeping the flow rate of each pump at 2.8 mL/min, which corresponds, depending on the temperature, to distinct residence time values. In the text, we refer to these samples with the labels T250, T300, T350, and T400. The list of parameters employed in these experiments is reported in Table 1.

Table 1
Experimental parameters employed during the synthesis at different temperatures of T250, T300, T350, and T400.

Sample name	T250	T300	T350	T400
Temperature (°C)	250	300	350	400
Pressure (MPa)	23.5	23.5	23.5	23.5
Residence time (s)	~ 115	~105	~ 88	~ 20

Powder X-ray diffraction patterns of the as-synthesized samples are shown in Fig. 2. The majority of the peaks in all samples are coincident in positions and intensities with those of xonotlite, as reported in PDF file no. 00–023–0125 of monoclinic xonotlite (space group P2/a) in the International Center for Diffraction Data (ICDD) database. Furthermore, the most intense diffraction peak, centered at 28.9° (2θ), is related to the (320) reflection in all the diffraction patterns.

Comparing the diffraction patterns of T250, T300, T350, and T400 samples, the effect of temperature is clear: higher temperature, despite the shorter time that growing particles spend in the reactor, increases the material crystallinity. T350 and T400 exhibit sharper and less broadened diffraction peaks compared to samples synthesized at a lower temperature. Furthermore, it is possible to observe that in these conditions of low flow rate (high residence time), the increase of the temperature leads to the crystallization of wollastonite (principal diffraction peak centered around 30° (2θ)) and calcium carbonate polymorphs, as calcite and vaterite. The presence of vaterite and wollastonite is responsible for broadening the (202) peak in T250 and T300, which at higher temperatures (T300 and T400) clearly shows three different diffraction peaks. At the same time, the diffraction peaks at 43.4°, 44.3°, and 50.4° (2θ) came from the sample holder in stainless steel.

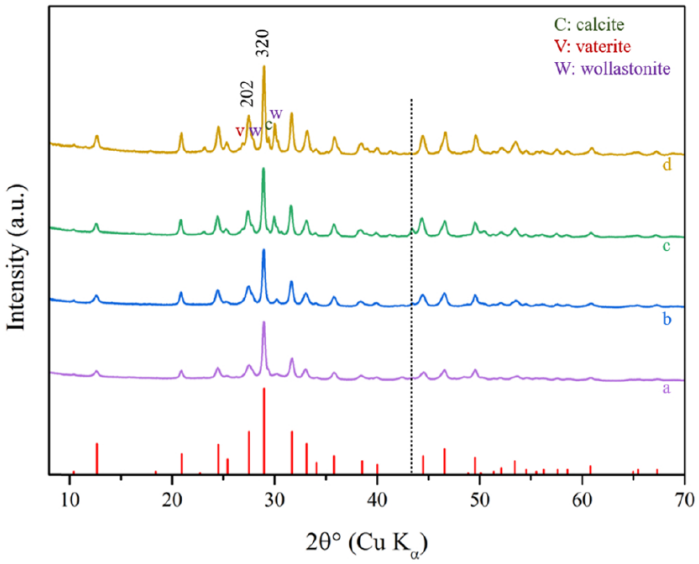

Fig. 2. Powder X-ray diffraction patterns of samples T250, T300, T350 and T400 synthesized under near- and supercritical conditions at 23.5 MPa and (a) 250 °C, (b) 300 °C, (c) 350 °C and (d) 400 °C, respectively. In red, the positions and intensities of the diffraction peaks as reported in PDF file no. 00–023–0125 of monoclinic xonotlite (space group P2/a) are shown. The letters C, V, and W indicate diffraction peaks of calcite, vaterite, or wollastonite phases, respectively. The vertical black dot line indicates diffraction from the stainless-steel sample holder.

These findings represent the first proof of xonotlite synthesis under near critical conditions (250–350 °C) in only tens of seconds in a continuous process. Even if the reaction yields and the samples' crystallinity are reduced compared to the specimen synthesized at 400 °C, these results at lower temperatures are very promising. Suffice it to say that several hours are required for the conventional hydrothermal synthesis at 250 °C [14]. In this way, for some applications that are not needed an excellent degree of crystallinity, the methodology developed in this work can represent a real innovation for the production of xonotlite.

The effect of temperature on the formation of xonotlite was further analyzed by investigating the local environment of protons at the atomic nearest neighbor and next-nearest neighbor scale. Fig. 3 displays the ^{1}H MAS NMR spectra of samples T250, T300, T350, and T400.

All the spectra show two peaks at 1.9 and 2.3 ppm, attributed to the presence of Si–OH and Ca–OH groups, respectively. In contrast, the broad signal around 5 ppm can be assigned to molecular water adsorbed on the mineral particle surface. Although xonotlite's ideal crystal structure should contain only Ca–OH units like in portlandite, previous studies have shown deviations from the ideal model [14]. As a consequence, our results are in agreement with the existence of two different types of proton environments already detected in both natural and synthetic xonotlite produced under conventional hydrothermal conditions [15], [29], [30], [31].

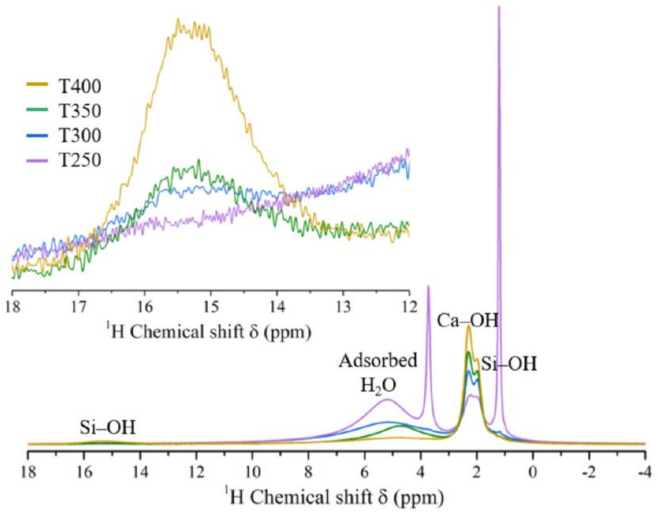

Fig. 3. ^{1}H MAS NMR spectra of samples T250, T300, T350, and T400 synthesized under near- and supercritical conditions at 23.5 MPa and 250, 300, 350, and 400 °C, respectively. The spectra are normalized for the material mass and the number of scans and thus comparable to each other. The inset shows a zoom in the range within 12 and 18 ppm of the spectra.

Furthermore, the spectrum of the sample T250 shows two more intense peaks at 1.2 and 3.7 ppm, which can be assigned to the presence of unreacted C-S-H precursor due to the low synthesis temperature. Small contributions of these peaks are also observed in the sample T300. The inset in Fig. 3 shows that another peak at around 15 ppm appears by increasing the temperature. This signal can be assigned to strongly hydrogen-bonded protons involving Si–OH groups, as already reported for other silicate minerals [32]. From the deconvolution of the spectra, this contribution has been calculated to be equal to 5% in T400, and around 1–2% in T300 and T350, whereas it was not detected in T250.

More information can be obtained from the comparison between these spectra. First, by increasing the temperature, the quantity of xonotlite in the sample increases (especially, the amount of Ca–OH increases), NMR giving semi-quantitative information. That result agrees with the PXRD analyses of the previously reported samples. Second, the quantity of molecular water adsorbed on the mineral surface decreases. Third, the peak at around 15.2 ppm becomes more intense the higher the temperature is. These findings suggest that higher temperature and thus higher structure crystallinity increase the H-bond network strength and a lower wettability of the mineral surface.

The silicate structure and the local chemical environment of Si atoms in xonotlite samples, synthesized at different temperatures, were investigated by ^{29}Si MAS NMR. To interpret the results, we must recall the structure of this mineral phase. As shown in Fig. 4(a), three different silicon sites are present in the silicate chains of xonotlite. Among them, two are in bridging positions, Si(1) and Si(2), and the third one is located in a branching place, Si(3). Consequently, three contributions, namely Q^2_H, Q^2_L, and Q^3, appear in the SSNMR xonotlite spectrum. The presence of two Q^2 components is because the bridging Si atoms have different Si–O bond lengths and Si–O–Si bond angles, in agreement with the model proposed by Kudoh and Takeuchi [15]. In Fig. 4(b), the signal centered around − 86 ppm is attributed to the Q^2 Si sites, and the other at − 97 ppm to the presence of Q^3 silicon tetrahedra in branching position. We can observe that splitting the Q^2 peak into two components becomes much clearer at high temperatures; on the contrary, it is less detectable due to the broadening of the signals when decreasing the temperature. The sharpness of SSNMR peaks in

T350 and T400 samples prove their higher crystallinity, in agreement with the PXRD results. Furthermore, another peak appears in T250 and T300 at around − 80 ppm due to the Q^1 contribution related to the end site of the silicate anion chains.

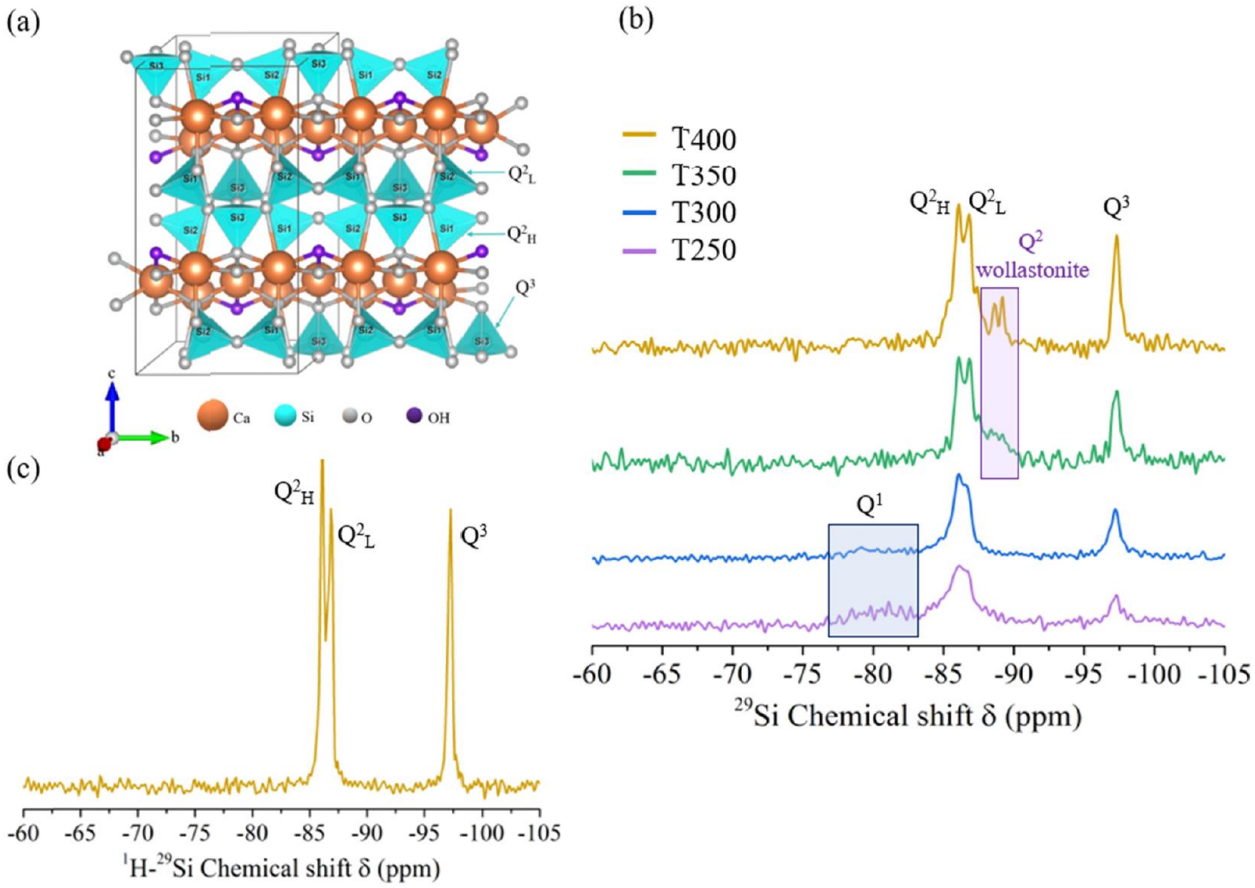

Fig. 4. (a) Crystal structure of xonotlite determined from the crystallographic information framework (CIF) file reported by Kudoh et al. [15] in the NIST Inorganic Crystal Structure Database (ICSD) [33]. In the structure, the Si(1), Si(2), and Si(3) atoms, which give rise to three different contributions (Q^2_H, Q^2_L and Q^3) to the SSNMR xonotlite spectrum can be distinguished. The black rectangle represents the limits of the unit cell. (b) ^{29}Si MAS NMR spectra of samples T250, T300, T350, and T400 synthesized under near- or supercritical conditions at 23.5 MPa and 250, 300, 350, and 400 °C, respectively. The spectra are normalized for the material mass and the number of scans and thus comparable to each other. (c) ^{1}H–^{29}Si CP/MAS NMR spectrum of T400.

The presence of Q^1 Si sites is the direct evidence of defects and a more defective and low crystalline material. In this sense, it is interesting to observe that the Q^1 contribution decreases by increasing the temperature. On the other hand, the spectra of samples synthesized at higher temperatures, T350 and T400, show another signal at around − 88 ppm, which can be associated with the wollastonite presence in the samples. The proof that this contribution comes from wollastonite was obtained through the ^{1}H–^{29}Si CP/MAS NMR experiment, which is sensitive only to Si in close proximity to H atoms. Being protons absent in wollastonite structure, ^{1}H–^{29}Si CP/MAS NMR spectrum of T400 does not exhibit the peak a − 88 ppm, Fig. 4(c). In this sense, SSNMR confirms the formation of wollastonite in T350 and T400, already observed by powder X-ray diffraction.

The morphology of xonotlite crystals continuously synthesized at different process conditions was investigated by HR-SEM. As shown in Fig. 5, the mineral phase exhibits a fiber-like morphology. Especially, it is possible to observe that although fibers present a wide distribution in size, increasing the temperature from 250 °C to 400 °C, they tend to be longer and less wide. This result could be explained by taking into account the work of Zou et al. [26]. They observed that by performing xonotlite synthesis at 240 °C, extending

the synthesis time from 6 to 48 h, the fibers split into thinner separated units. In our case, the ultra-fast kinetics of SHFS could favor the growth of the fiber along the silicates chains, resulting in longer particles that splitting into many units less wide.

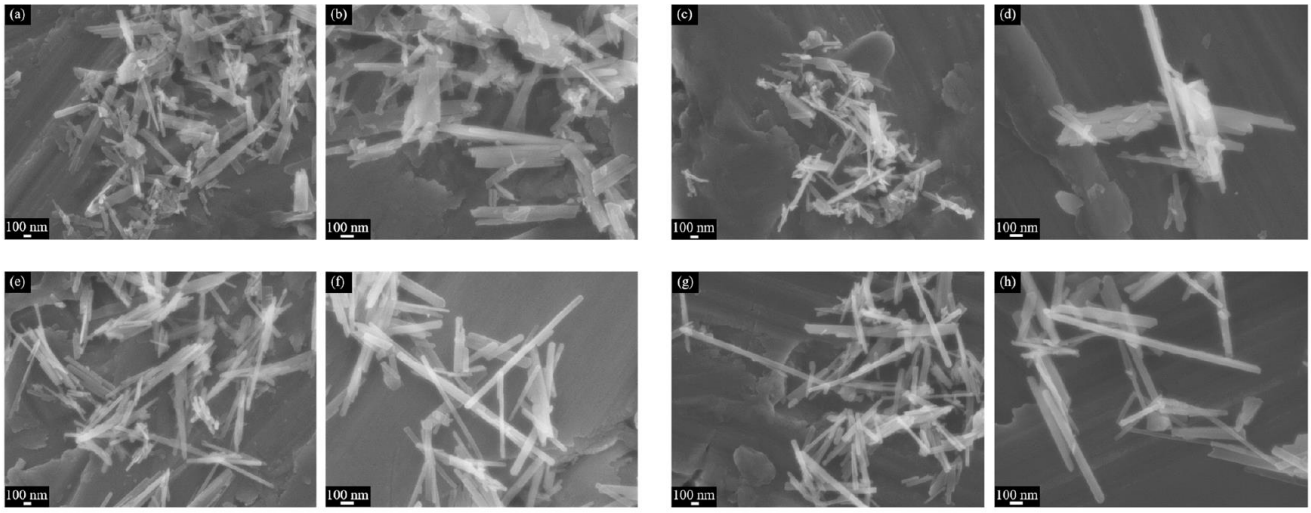

Fig. 5. HR-SEM images at different magnifications (30,000 × or 50,000 ×) of: (a) and (b) T250, (c) and (d) T300, (e) and (f) T350, (g) and (h) T400 synthesized under near- and supercritical conditions at 23.5 MPa and 250, 300, 350, and 400 °C, respectively. Both aggregates of small fibers as well as large single units are present.

3.1.2. Influence of residence time

To avoid as much as possible the crystallization of wollastonite and obtain single-phase xonotlite, the synthesis was performed at 400 °C, and 25 MPa, reducing the residence time down to 7 s. In Fig. 6, the PXRD pattern of this sample shows well-defined diffraction peaks corresponding, in positions and intensities, to those reported in PDF file no. 00–023–0125 of monoclinic xonotlite. Under these synthesis conditions, the presence of wollastonite is reduced to a neglectable amount.

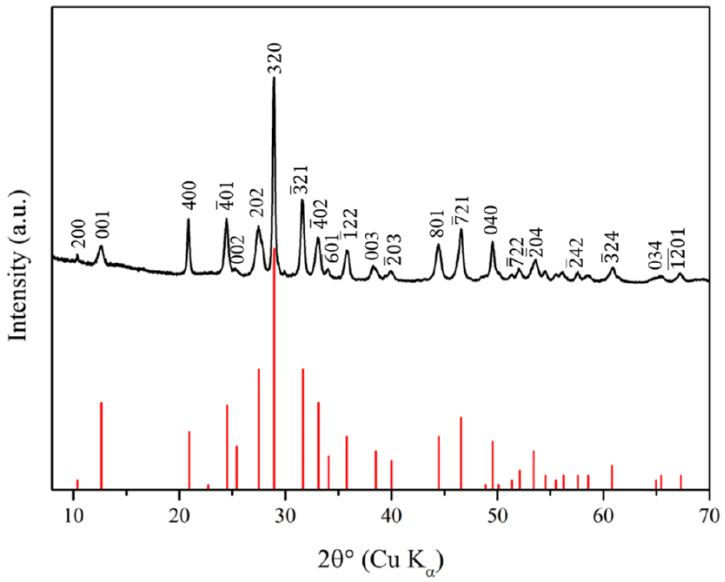

Fig. 6. Powder X-ray diffraction pattern of xonotlite synthesized under supercritical conditions at 25 MPa, 400 °C, and 7 s. In red, the positions and intensities of the diffraction peaks as reported in PDF file no. 00–023–0125 of monoclinic xonotlite (space group P2/a) are shown. Each peak is identified by the corresponding Miller indices as reported in PDF file no. 00–023–0125.

Xonotlite synthesized under sub- or supercritical conditions mainly consist of tiny flat fibers [34], [35], [36]. HR-TEM analysis was performed to get information on the preferential growing direction of the crystals. Fig. 7(a) and (b) show well crystalline xonotlite fibers, which confirm the PXRD results. It is possible to observe the (2,0,0) atomic planes (Fig. 7(b)) characteristic of the xonotlite structure, suggesting that the fiber grows along the direction of the silicate chains parallel to the b-axis (Fig. 7(d)). The interlayer distance between these planes was measured to be equal to 8.6 Å (Fig. 7(c)) in agreement with the (200) reflection observed in the PXRD pattern.

To study the effect of the residence time shortening (from 20 down to 7 s) on the silicate structure of xonotlite, ^{29}Si MAS NMR was performed, Fig. 8. The ^{29}Si MAS NMR spectrum of xonotlite synthesized in supercritical water in only 7 s shows three signals assigned to Q^2_H, Q^2_L, and Q^3, agreeing with the silicate structure xonotlite reported in Fig. 4(a). The areas of Q^2 and Q^3 signals were calculated through the deconvolution of the peaks. The ratio between the areas, Q^2:Q^3 was approximately 2:0.9. However, the ideal crystal structure of xonotlite is built by parallel silicate chains in “dreiereinfachketten” arrangement with two “paired” Q^2 tetrahedra (Si(1), Si(2)) and one Q^3 site (Si(3)); consequently, Q^2:Q^3 ratio should be equal to 2:1. That difference implies that in xonotlite synthesized under supercritical conditions, some Q^3 silicon sites are missing. Similar results were also found in other studies on synthetic and natural xonotlite[37]. Furthermore, the absence of wollastonite in this sample, as previously observed by PXRD, is confirmed by ^{29}Si MAS NMR, as the peak characteristic for the dehydrated phase at − 88 ppm is not anymore detectable if compared to Fig. 4(b).

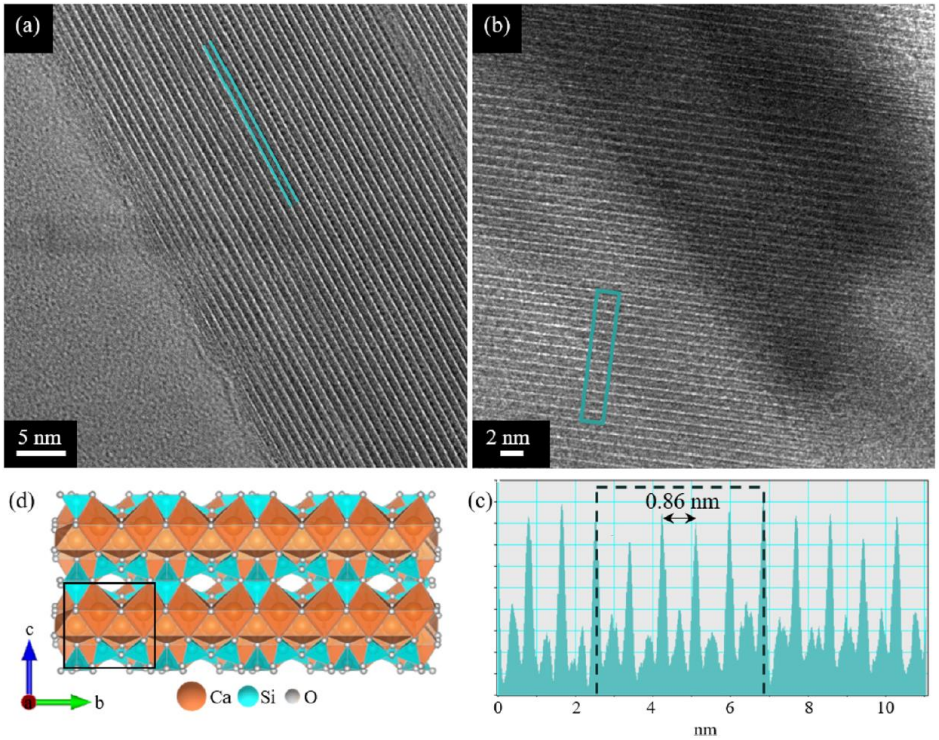

Fig. 7. (a) and (b) HR-TEM images of xonotlite fibers, synthesized under supercritical conditions, show the material’s ordered and well-arranged crystal lattice. (c) Distance profile derived from the light blue region in (b) to measure the interlayer distance between planes related to reflection (200) and perpendicular to the fiber’s length. (d) Crystal structure of xonotlite as reported in the CIF file disclosed by Hejny et al. [16] in the NIST Inorganic Crystal Structure Database [33].

Another technique that gives detailed information on the chemical structure of a mineral is infrared spectroscopy. The characteristic IR spectrum of xonotlite is shown in Fig. 9. The spectrum, acquired in the range 1800–400 cm $^{-1}$, can be divided into two groups of bands related to vibrations of (i) water molecules, and (ii) octahedral Ca and tetrahedral Si, as commonly observed in calcium silicate hydrates [30], [38].

The peak at 1632 cm^{-1} is attributed to the scissoring bending mode of water [38]. Instead, the bending mode vibration of CaO–H, typical of xonotlite structure, is observed at 631 cm^{-1}. The band around 1202 cm^{-1} is assigned to Si–O stretching vibrations involving Q^3 branching sites ((Si–O)Q^3) [38]. The spectral features of silicates, which appear around 978 and 930 cm^{-1} are attributed to Si–O stretching of Q^2 sites ((Si–O)Q^2).

It is worth mentioning that in the spectrum does not appear the vibration band (Si–O)Q^1, commonly detected around 828 cm^{-1} [38], confirming the SSNMR results. The signal observed at 1088 cm^{-1} could be assigned to the asymmetric (ν_{as}(Si–O–Si)) vibration of Si–O–Si bridges; the respective symmetric stretching bands (ν_s(Si–O-Si)) appear at 672 and 610 cm^{-1}. Lastly, the band at 536 cm^{-1} is assigned to Si–O–Si bending mode (δ_s (Si–O–Si)); on the contrary, the O–Si–O bending mode (δ_s (O–Si–O)) appear at 456 cm^{-1} [38]. Although no peaks related to carbonates were observed in the diffraction pattern, in the IR spectrum of xonotlite, small contributions related to CO_3^{2-} vibration bands were detected and marked with an asterisk. The presence of small carbonate traces in xonotlite is commonly reported in the literature [38].

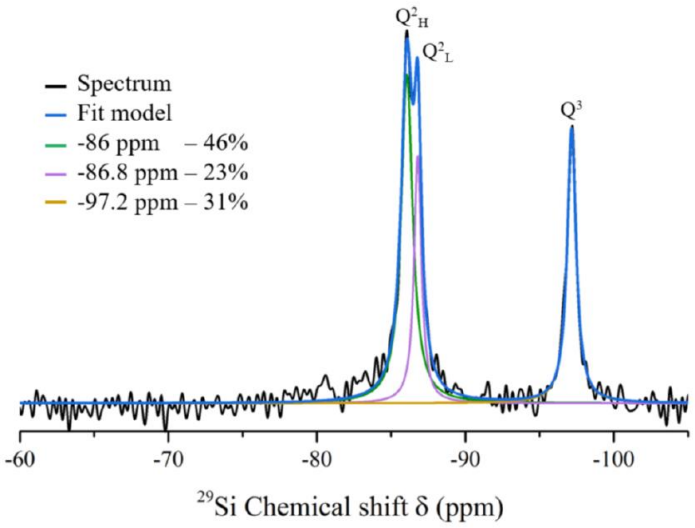

Fig. 8. ^{29}Si MAS NMR spectrum of xonotlite synthesized under supercritical conditions at 25 MPa and 400 °C in 7 s.

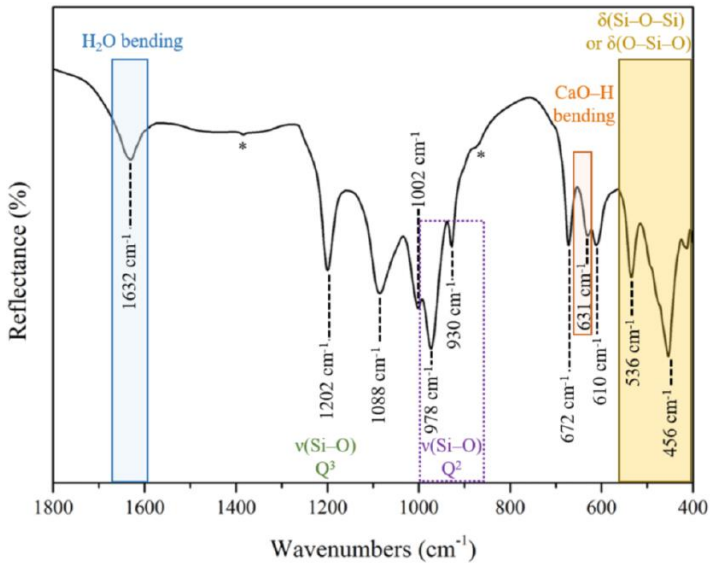

Fig. 9. IR spectrum of xonotlite synthesized in supercritical water at 25 MPa and 400 °C in 7 s. The asterisks denote CO_3^{2-} vibration bands related to carbonate impurity.

So far, the results related to xonotlite crystallization via a near- and supercritical hydrothermal flow synthesis were presented. Our findings have shown that temperature, residence time, and pressure play a fundamental role in the synthesis process, highlighting the importance of controlling the reaction kinetics to avoid secondary phases. Xonotlite nanoparticles synthesized at 25 MPa, 400 °C in 7 s show fiber-like morphology and well-crystallized structure. After the investigation of the structure, the physicochemical properties, and the morphology, in the following, we will focus on the employment of xonotlite synthesized via an SHFS into the application of a cement-based material.

3.2. Application of the as-synthesized xonotlite particles

3.2.1. Calorimetric test

Within the frame of this work, calorimetry analysis was used as a sensitive tool for studying the exothermic hydration process of cement over time. The heat evolution is strongly correlated to the rate of the chemical reactions that take place during hydration, and chemical additions influence it. Consequently, the effect of xonotlite particles as seeds can be detected by monitoring the hydration curve changes. In Fig. 10(a), the first exothermic peak is associated with the precipitation of the main hydration products, C-S-H gel, and portlandite. Later, a second peak corresponds to the precipitation of ettringite and the dissolution of C_3A [39].

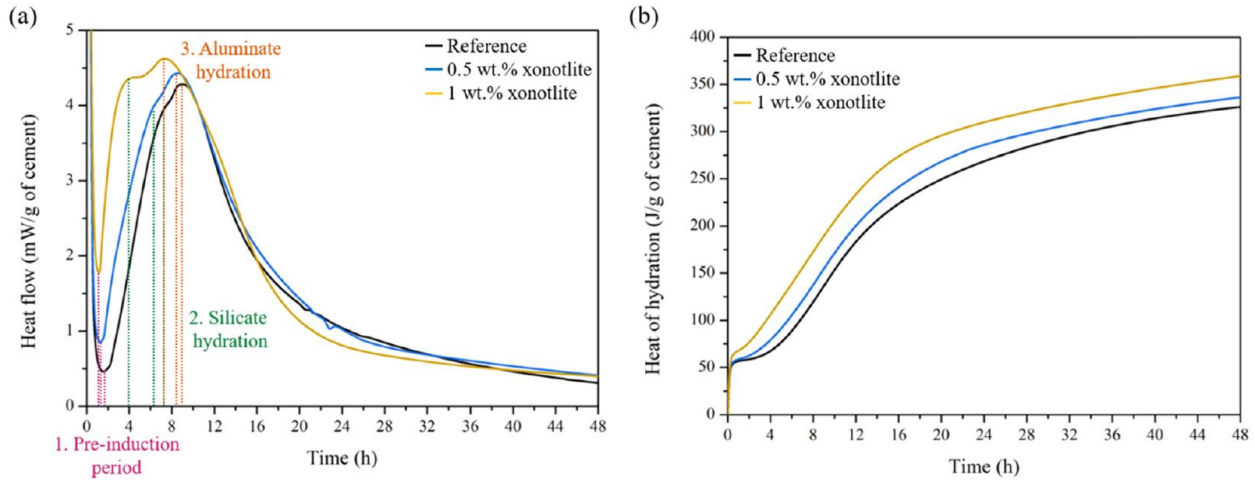

Fig. 10. (a) Heat flow and (b) cumulative heat measured over time during the hydration of reference cement paste and seeded cement pastes (xonotlite addition 0.5 and 1 wt%).

To evaluate the accelerating behavior of xonotlite, the position of the heat flow maximum, t_{max} (in hours), at the end of the acceleration period was determined [40]. A heat flow maximum that occurs earlier than in the reference sample can be defined as an acceleration of the cement hydration. In Fig. 10(a), the reference sample shows the longest pre-induction period, while increasing xonotlite dosage gradually accelerates that period. Additionally, the induction period is essentially eliminated when 1 wt% of xonotlite is added into the paste. This phenomenon is due to the larger number of available nuclei for the hydration product growth from time zero. Furthermore, the seed addition promotes faster calcium, hydroxyl, and silicate species saturation, contributing to the achievement of the supersaturation state in the solution in a shorter period of time. In turn, this phenomenon leads to the earlier C-S-H precipitation, promoting the earlier starting of acceleration period compared to the case of the reference sample. In particular, the onset of C-S-H gel and portlandite formation from the silicate hydration appears after ~ 70 and 80 min for the cement paste prepared with 0.5 wt% and 1 wt% of xonotlite addition, respectively.

At the same time, the onset of the silicate hydration of cement paste used as reference occurs at ~100 min Fig. 10(a) shows that the gain in heat flow after the induction period is much faster when the particle dosage increases. The shoulder of silicate hydration occurs earlier in seeded cement pastes, at ~4 h and ~6.2 h with an addition of 0.5 and 1 wt% respectively, if compared with the reference paste where it appears after ~ 7.5 h. Although, the heat flow maximum related to silicate hydration increases significantly in both seeded pastes of ~2.5% and ~9.5% in respect to the unseeded sample. This phenomenon is related to the higher number of hydration product regions that grow simultaneously. Additionally, the cement pastes prepared with xonotlite seeds have accelerated aluminate hydration.

The peak related to this process for cement paste containing 1 wt% of xonotlite is shifted to ~2 h earlier, and its height increased by 8% if compared with the calorimetric curve of the reference sample. That acceleration is related to an earlier calcium sulfoaluminate hydrate (AFt) depletion and might be due to stronger calcium and hydroxide ion flows when seeds are added, as previously proposed by Nicoleau et al. [41], [42]. It is worth mentioning that, despite this acceleration, the silicate peaks appear earlier than that of aluminate; contrarily, the over-accelerated hydration of aluminate would suppress that one of silicate, disturbing the strength gain of seeded cement at the early age [7], [43].

The total heat released during the early nucleation and growth period, Fig. 10(b), is more significant in seeded pastes. The xonotlite additions allow the hydration product to nucleate in the pore space between the particles reducing the capillary porosity, as reported in the model by Thomas et al. [44]. In particular, the total generated heat during 48 h hydration of 0.5 wt% and 1 wt% seeded pastes were ~3.5% and 11% higher than the reference, respectively. This result is promising if compared with that of other semicrystalline C-S-H seeds. Wang et al. have reported that the acceleration effect related to 1 wt% of nanometric C-S-H particles (Ca/Si molar ratio = 1) was not sustained up to 48 h [45]. With this material, they observed the same total heat release in the reference and seeded pastes after 48 h. These results imply that xonotlite synthesized by SHFS, besides influencing the C-S-H gel nucleation, continues affecting the hydration process after tens of hours.

3.2.2. X-ray computed microtomography analysis

Based on the calorimetry results, the X-ray computed microtomography measurements have been performed at two different hydration times: 7 and 36 h. In this way, the first analysis allows investigating the effect of xonotlite on the acceleration of the silicate hydration with respect to the reference sample. On the other hand, the second measurement verifies if the acceleration effect is sustained up to longer hydration times. The acceleration effect of xonotlite on cement hydration, already observed by calorimetry analysis, was further confirmed by X-ray computed microtomography. In Fig. 11, the seeded paste with 1 wt% of xonotlite exhibit a lower fraction of unreacted material (in orange), especially the large anhydrate cement particles compared to the reference specimen at the same hydration age, 7 h.

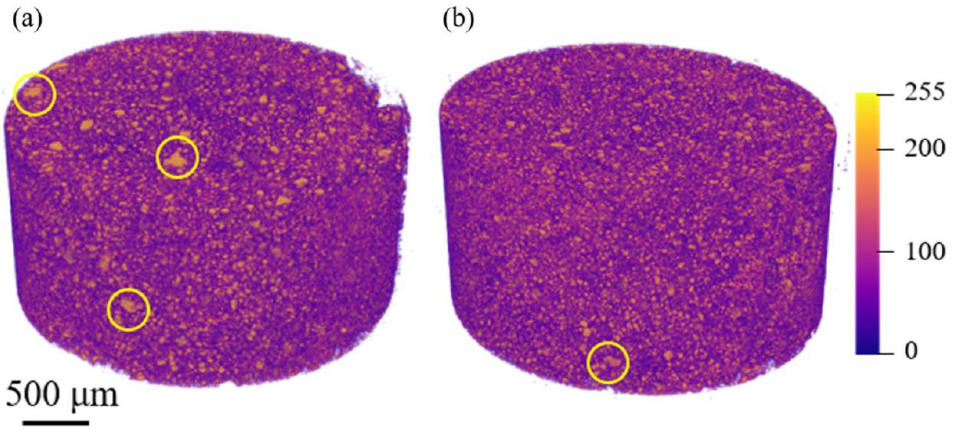

Fig. 11. Visualization of the reconstructed 3D µCT images of (a) reference sample and (b) 1 wt% xonotlite seeded cement pastes obtained with Tomviz. The µCT tomograms were acquired at 7 h of hydration for all samples. Yellow circles indicate unhydrated clinker particles, which appear bigger in size in the reference sample than in the seeded aste (For interpretation of the references to colour in this figure legend, the reader is referred to the web version of this article.).

The accelerated kinetics of cement hydration induced by seed addition was further investigated by analyzing the evolution and depletion of the unhydrated phase over time. First, a 3D bilateral filter was applied on the reconstructed tomograms to enhance the phase contrast between unhydrated phase, hydration phase, and pore phase [46], [47]. Then, Ostu algorithm [7], [48] was utilized to segment the unhydrated phase, and the segmented volumes of unhydrated phase were in good agreement with the observed unnhydrated particles in Fig. 10, which verified the accuracy of the phase segmentation. Further morphological measurements [49] of the volume and mean radius of segmented unhydrated particles, in this research, were conducted based on the segmented unhydrated phase. Table 2 gives the total volume and mean radius of unhydrated particles for reference and seeded pastes. These comparisons show that at the same hydration age, 7 h, the seeded

pastes exhibit a lower content of unreacted particles. Such unhydrated particles also have a smaller mean radius in seeded sample than those in the reference sample, which verifies the acceleration of hydration in seeded sample.

Table 2
Values of total unhydrated volume (μm^3) and mean radius of unhydrated particles (μm) measured through the statistical analysis performed on reference sample, and 1 wt% xonotlite seeded paste after 7 h of hydration.

	Total unhydrated volume (μm^3)	Mean radius of unhydrated particles (μm)
Reference	$\sim 2.7 \cdot 10^9$	~ 5.9
1 wt% xonotlite	$\sim 2.2 \cdot 10^9$	~ 3.9

Therefore, it can be stated that the introduction of xonotlite seeds influences the early hydration kinetics. Studying the hydration effect over time, we have observed that the seeds sustain the acceleration effect up to 36 h, as previously detected through calorimetric measurements. In fact, at that age of hydration, Table 3, the seeded paste exhibits a lower volume of unhydrated phase, confirming the earlier depletion of unhydrated particles to form the hydrated products.

Table 3
Values of total unhydrated volume (μm^3) and mean radius of unhydrated particles (μm) measured through the statistical analysis performed on reference sample, and 1 wt% xonotlite seeded paste after 36 h of hydration.

	Total unhydrated volume (μm^3)	Mean radius of unhydrated particles (μm)
Reference	$\sim 1.9 \cdot 10^9$	~ 3.6
1 wt% xonotlite	$\sim 1.6 \cdot 10^9$	~ 2

To conclude, the difference between the mean diameters of unhydrated particles in the reference sample and the seeded paste is ~4 μm when 1 wt% of xonotlite is added after 7 h. At 36 h of hydration, these differences between diameters decrease down to ~3.2 μm. It is worth mentioning that the spatial resolution in measuring the diameters of unhydrated particles is 1.3 μm/pixel. In these experiments, the main factors that can cause errors in the results are: (i) the limitation of the μCT resolution and (ii) the image segmentation procedure.

4. Conclusions

This study has investigated the effect of several experimental parameters on the near- and supercritical hydrothermal flow synthesis of xonotlite. Our findings have shown that temperature, residence time, and pressure play a fundamental role in the synthesis process, highlighting the importance of controlling the reaction kinetics to avoid secondary phases or amorphous products. For the first time, we have shown that the formation of this mineral takes place in a wide range of temperatures, from 250° to 350°C at 23.5 MPa in only tens of seconds. Based on these findings, it appears clear the interest in using the SHFS as a fast, profitable, and scalable manufacturing route for producing synthetic xonotlite fibers to replace the very long conventional hydrothermal methodology. Furthermore, we have demonstrated that under supercritical

conditions (400 °C and 25 MPa) single phase of high crystalline xonotlite can be produced (i.e. without the presence of secondary phases), just reducing the residence time down to 7 s. As a conclusion of these results, it can be stated that the supercritical hydrothermal flow synthesis allows producing perfect model nanominerals by mimicking natural environments at high temperatures and pressures.

Finally, we have explored the possible application of xonotlite additions in cement-based materials. Our results obtained through calorimetry and X-ray microtomography analyses have shown that xonotlite particles can act as nucleation points that trigger the quick and autocatalytic formation of C-S-H gel. The acceleration of cement hydration allows the development of faster, denser, and stronger cement paste, which from an application point of view permits to reduce the time and the costs of construction. Based on these findings, future works could investigate the effect of other crystalline CSH nanoparticles synthesized via SHFS with different Ca/Si ratios and specific surface areas.

Declaration of Competing Interest

The authors declare that they have no known competing financial interests or personal relationships that could have appeared to influence the work reported in this paper.

Acknowledgments

This work was carried out under the umbrella of the Bordeaux-Euskampus Euro-regional Campus of International Excellence initiative and supported by the International Doctoral Program developed between the University of Bordeaux (UB) and the University of the Basque Country (UPV/EHU). This work was also performed in the frame of the LTC Green Concrete. Valentina Musumeci is grateful to the Initiative of Excellence (IdEX) of the University of Bordeaux for financial support. The authors also acknowledge CNRS, Bordeaux INP, and Région Nouvelle-Aquitaine for their financial support.

References

[1] M. Claverie, M. Diez-Garcia, F. Martin, C. Aymonier. **Continuous synthesis of nanominerals in supercritical water.** Chem. Eur. J., 25 (2019), pp. 5814-5823, 10.1002/chem.201805435

[2] X. Li, J. Chang. **A novel hydrothermal route to the synthesis of xonotlite nanofibers and investigation on their bioactivity.** J. Mater. Sci., 41 (2006), pp. 4944-4947, 10.1007/s10853-006-0305-3

[3] G. Wei, Y. Liu, X. Zhang, F. Yu, X. Du. **Thermal conductivities study on silica aerogel and its composite insulation materials.** Int. J. Heat Mass Transf., 54 (2011), pp. 2355-2366, 10.1016/j.ijheatmasstransfer.2011.02.026

[4] N.M.P. Low, J.J. Beaudoin. **Mechanical properties and microstructure of cement binders reinforced with synthesized xonotlite micro-fibres.** Cem. Concr. Res., 23 (1993), pp. 1016-1028, 10.1016/0008-8846(93)90161-2

[5] Concrete needs to lose its colossal carbon footprint,2021. Nature. 597 (2021) 593–594. https://doi.org/10.1038/d41586–021-02612–5.

[6] Making Concrete Change: Innovation in Low-carbon Cement and Concrete, 2022. Chatham House – Int. Aff. Think Tank. (2018). https://www.chathamhouse.org/2018/06/making-concrete-change-innovation-low-carbon-cement-and-concrete (accessed February 21, 2022).

[7] J. Li, W. Zhang, K. Xu, P.J.M. Monteiro. **Fibrillar calcium silicate hydrate seeds from hydrated tricalcium silicate lower cement demand.** Cem. Concr. Res., 137 (2020), Article 106195, 10.1016/j.cemconres.2020.106195

[8] D. Hernández-Cruz, C.W. Hargis, J. Dominowski, M.J. Radler, P.J.M. Monteiro. **Fiber reinforced mortar affected by alkali-silica reaction: a study by synchrotron microtomography.** Cem. Concr. Compos., 68 (2016), pp. 123-130, 10.1016/j.cemconcomp.2016.02.003

[9] U. Sharma, L.P. Singh, B. Zhan, C.S. Poon. **Effect of particle size of nanosilica on microstructure of C-S-H and its impact on mechanical strength.** Cem. Concr. Compos., 97 (2019), pp. 312-321, 10.1016/j.cemconcomp.2019.01.007

[10] H. Li, C. Xu, B. Dong, Q. Chen, L. Gu, X. Yang. **Enhanced performances of cement and powder silane based waterproof mortar modified by nucleation C-S-H seed.** Constr. Build. Mater., 246 (2020), Article 118511, 10.1016/j.conbuildmat.2020.118511

[11] K. Sobolev, M.F. Gutierrez, How nanotechnology can change the concrete world, Am. Ceram. Soc. Bull. (n.d.) 1338–1355.

[12] P.J.M. Monteiro, G. Geng, D. Marchon, J. Li, P. Alapati, K.E. Kurtis, M.J.A. Qomi. **Advances in characterizing and understanding the microstructure of cementitious materials.** Cem. Concr. Res., 124 (2019), Article 105806, 10.1016/j.cemconres.2019.105806

[13] G. Land, D. Stephan. **Controlling cement hydration with nanoparticles.** Cem. Concr. Compos., 57 (2015), pp. 64-67, 10.1016/j.cemconcomp.2014.12.003

[14] M. Diez-Garcia, 2017. Synthesis by supercritical fluids methods of advanced additions for cementitious materials, Universidad del Pais Vasco and Univerité de Bordeaux, 2017.

[15] Y. Kudoh, Y. Takéuchi. **Polytypism of xonotlite: (I) structure of an A-1 polytype.** Mineral. J., 9 (1979), pp. 349-373, 10.2465/minerj.9.349

[16] C. Hejny, T. Armbruster. **Polytypism in xonotlite $Ca_6Si_6O_{17}(OH)_2$.** Z. Für Krist., 216 (2001), pp. 396-408, 10.1524/zkri.216.7.396.20363

[17] E. Spudulis, V. Šavareika, A. Špokauskas. **Influence of hydrothermal synthesis condition on xonotlite crystal morphology.** Mater. Sci., 19 (2013), pp. 190-196, 10.5755/j01.ms.19.2.4437

[18] K. Speakman. **The stability of tobermorite in the system CaO-SiO_2-H_2O at elevated temperatures and pressures.** Mineral. Mag., 36 (1968), pp. 1090-1103, 10.1180/minmag.1968.036.284.06

[19] A. Dumas, M. Claverie, C. Slostowski, G. Aubert, C. Careme, C. Le Roux, P. Micoud, F. Martin, C. Aymonier. **Fast-geomimicking using chemistry in supercritical water.** Angew. Chem., 128 (2016), pp. 10022-10025, 10.1002/ange.201604096

[20] C. Aymonier, A. Loppinet-Serani, H. Reverón, Y. Garrabos, F. Cansell. **Review of supercritical fluids in inorganic materials science.** J. Supercrit. Fluids, 38 (2006), pp. 242-251, 10.1016/j.supflu.2006.03.019

[21] C. Aymonier, G. Philippot, A. Erriguible, S. Marre. **Playing with chemistry in supercritical solvents and the associated technologies for advanced materials by design.** J. Supercrit. Fluids, 134 (2018), pp. 184-196, 10.1016/j.supflu.2017.12.021

[22] M. Diez-Garcia, J.J. Gaitero, J.I. Santos, J.S. Dolado, C. Aymonier. **Supercritical hydrothermal flow synthesis of xonotlite nanofibers.** J. Flow Chem., 8 (2018), pp. 89-95, 10.1007/s41981-018-0012-7

[23] A.A. MacDowell, D.Y. Parkinson, A. Haboub, E. Schaible, J.R. Nasiatka, C.A. Yee, J.R. Jameson, J.B. Ajo-Franklin, C.R. Brodersen, A.J. McElrone, 2012. X-ray micro-tomography at the Advanced Light Source, in: Dev. X-Ray Tomogr. VIII, International Society for Optics and Photonics, 2012: p. 850618. https://doi.org/10.1117/12.930243.

[24] D. Gürsoy, F. De Carlo, X. Xiao, C. Jacobsen. **TomoPy: a framework for the analysis of synchrotron tomographic data.** J. Synchrotron Radiat., 21 (2014), pp. 1188-1193, 10.1107/S1600577514013939

[25] W. Kanitpanyacharoen, D.Y. Parkinson, F. De Carlo, F. Marone, M. Stampanoni, R. Mokso, A. MacDowell, H.-R. Wenk. **A comparative study of X-ray tomographic microscopy on shales at different synchrotron facilities: ALS, APS and SLS.** J. Synchrotron Radiat., 20 (2013), pp. 172-180, 10.1107/S0909049512044354

[26] J. Zou, C. Guo, Y. Jiang, C. Wei, F. Li. **Structure, morphology and mechanism research on synthesizing xonotlite fiber from acid-extracting residues of coal fly ash and carbide slag.** Mater. Chem. Phys., 172 (2016), pp. 121-128, 10.1016/j.matchemphys.2016.01.050

[27] S. Shaw, S.M. Clark, C.M.B. Henderson. **Hydrothermal formation of the calcium silicate hydrates, tobermorite (Ca5Si6O16(OH)$_2$·4H2O) and xonotlite ($Ca_6Si_6O_{17}(OH)_2$): an in situ synchrotron study.** Chem. Geol., 167 (2000), pp. 129-140, 10.1016/S0009-2541(99)00205-3

[28] G.L. Kalousek, T. Mitsuda, H.F.W. Taylor. **Xonotlite: cell parameters, thermogravimetry and analytical electron microscopy.** Cem. Concr. Res., 7 (1977), pp. 305-312, 10.1016/0008-8846(77)90093-X

[29] Wiley Online Library, (n.d.). 〈https://ceramics.onlinelibrary.wiley.com/doi/abs/10.1111/j.1151–2916.1957.tb12579.x〉 (Accessed January 24, 2021).

[30] S.V. Churakov, P. Mandaliev. **Structure of the hydrogen bonds and silica defects in the tetrahedral double chain of xonotlite.** Cem. Concr. Res., 38 (2008), pp. 300-311, 10.1016/j.cemconres.2007.09.014

[31] F. Méducin, B. Bresson, N. Lequeux, M. de Noirfontaine, H. Zanni. **Calcium silicate hydrates investigated by solid-state high resolution 1H and 29Si nuclear magnetic resonance.** Cem. Concr. Res., 37 (2007), pp. 631-638, 10.1016/j.cemconres.2007.01.011

[32] F. Brunet, P. Bertani,, T. Charpentier, A. Nonat, J. Virlet. **Application of 29Si homonuclear and 1H–29Si heteronuclear NMR correlation to structural studies of calcium silicate hydrates.** J. Phys. Chem. B., 108 (2004), pp. 15494-15502, 10.1021/jp031174g

[33] NIST Inorganic Crystal Structure Database, National Institute of Standards and Technology, NIST Inorganic Crystal Structure Database, NIST Standard Reference Database Number 3, Gaithersburg MD. 20899 (n.d.).

[34] K. Lin, J. Chang, G. Chen, M. Ruan, C. Ning. **A simple method to synthesize single-crystalline β-wollastonite nanowires.** J. Cryst. Growth, 300 (2007), pp. 267-271, 10.1016/j.jcrysgro.2006.11.215

[35] V. Musumeci, A supercritical water-based technology for calcium silicate hydrate nanoparticles production, University of Bordeaux and University of the Basque Country, 2021.

[36] V. Musumeci, G. Goracci, P. Sanz Camacho, J.S. Dolado, C. Aymonier. **Correlation between the dynamics of nanoconfined water and the local chemical environment in calcium silicate hydrate nanominerals.** Chem. Eur. J. (2021), 10.1002/chem.202100098

[37] Noma Hiroaki, Adachi Yoshio, Matsuda Yoshihisa, Yokoyama Takushi. **29Si and 1H NMR of natural and synthetic xonotlite.** Chem. Lett. (2003), 10.1246/cl.1998.219

[38] ScienceDirect, (n.d.). https://www-sciencedirect-com.docelec.u-bordeaux.fr/science/article/pii/S092583880702249?via%3Dihub (Accessed October 18, 2021).

[39] H.F.W. Taylor. **Cement Chemistry.** Thomas Telford (1997), 10.1680/cc.25929

[40] ScienceDirect, (n.d.). 〈https://www-sciencedirect-com.docelec.u-bordeaux.fr/science/article/pii/S0958946516303845〉 (Accessed October 20, 2021).

[41] L. Nicoleau. **The acceleration of cement hydration by seeding: influence of the cement mineralogy** ZKG Int. (2013), pp. 40-49.

[42] L. Nicoleau, T. Gädt, L. Chitu, G. Maier, O. Paris. **Oriented aggregation of calcium silicate hydrate platelets by the use of comb-like copolymers.** Soft Matter, 9 (2013), pp. 4864-4874, 10.1039/C3SM00022B

[43] D. Marchon, R.J. Flatt. **12 - Impact of Chemical Admixtures on Cement Hydration.** P.-C. Aïtcin, R.J. Flatt (Eds.), Science technology concrete admixtures, Woodhead Publishing (2016), pp. 279-304, 10.1016/B978-0-08-100693-1.00012-6

[44] J.J. Thomas, H.M. Jennings, J.J. Chen. **Influence of nucleation seeding on the hydration mechanisms of tricalcium silicate and cement.** J. Phys. Chem. C., 113 (2009), pp. 4327-4334, 10.1021/jp809811w

[45] H. Wang, Q. Zhang, H. Yang, H. Sun. **Synthesis and microwave dielectric properties of $CaSiO_3$ nanopowder by the sol–gel process.** Ceram. Int., 34 (2008), pp. 1405-1408, 10.1016/j.ceramint.2007.05.001

[46] D. Ushizima, D. Parkinson, P. Nico, J. Ajo-Franklin, A. MacDowell, B. Kocar, W. Bethel, J. Sethian, 2011. Statistical segmentation and porosity quantification of 3D x-ray microtomography, in: Appl. Digit. Image Process. XXXIV, SPIE, 2011: pp. 11–24. https://doi.org/10.1117/12.892809.

[47] D. Ushizima, K. Xu, P.J.M. Monteiro. **Materials data science for microstructural characterization of archaeological concrete.** MRS Adv., 5 (2020), pp. 305-318, 10.1557/adv.2020.131

[48] N. Otsu. **A threshold selection method from gray-level histograms.** IEEE Trans. Syst. Man Cybern., 9 (1979), pp. 62-66, 10.1109/TSMC.1979.4310076

[49] K. Xu, A.S. Tremsin, J. Li, D.M. Ushizima, C.A. Davy, A. Bouterf, Y.T. Su, M. Marroccoli, A.M. Mauro, M. Osanna, A. Telesca, P.J.M. Monteiro. **Microstructure and water absorption of ancient concrete from Pompeii: an integrated synchrotron microtomography and neutron radiography characterization.** Cem. Concr. Res., 139 (2021), Article 106282, 10.1016/j.cemconres.2020.106282